A free-form prediction for the reappearance of supernova Refsdal in the Hubble Frontier Fields cluster MACSJ1149.5+2223

Jose M. Diego,[1][*] Tom Broadhurst,[2,3] Cuncheng Chen,[4] Jeremy Lim,[4] Adi Zitrin,[5][†]
Brian Chan,[4] Dan Coe,[6] Holland C. Ford,[6] Daniel Lam[4] and Wei Zheng[6]

[1]*IFCA, Instituto de Física de Cantabria (UC-CSIC), Av. de Los Castros s/n, E-39005 Santander, Spain*
[2]*Fisika Teorikoa, Zientzia eta Teknologia Fakultatea, Euskal Herriko Unibertsitatea UPV/EHU, E-48080 Bilbao, Spain*
[3]*IKERBASQUE, Basque Foundation for Science, Alameda Urquijo 36-5, E-48008 Bilbao, Spain*
[4]*Department of Physics, The University of Hong Kong, 0000-0002-6536-5575, Pokfulam Road, Hong Kong*
[5]*Cahill Center for Astronomy and Astrophysics, California Institute of Technology, MS 249-17, Pasadena, CA 91125, USA*
[6]*Department of Physics and Astronomy, Johns Hopkins University, Baltimore, MD 21218, USA*

ABSTRACT

The massive cluster MACSJ1149.5+2223($z = 0.544$) displays five very large lensed images of a well-resolved spiral galaxy at $z_{\rm spect} = 1.491$. It is within one of these images that the first example of a multiply lensed supernova (SN) has been detected recently as part of the Grism Lens-Amplified Survey from Space. The depth of this data also reveals many H II regions within the lensed spiral galaxy which we identify between the five counter-images. Here, we expand the capability of our free-form method to incorporate these H II regions locally, with other reliable lensed galaxies added for a global solution. This improved accuracy allows us to estimate when the Refsdal SN will appear within the other lensed images of the spiral galaxy to an accuracy of $\sim$7 per cent. We predict this SN will reappear in one of the counter-images (RA = 11:49:36.025, Dec. = +22:23:48.11, J2000) and on 2015 November 1 (with an estimated error of $\pm$25 d) it will be at the same phase as it was when it was originally discovered, offering a unique opportunity to study the early phases of this SN and to examine the consistency of the mass model and the cosmological model that have an impact on the time delay prediction.

Key words: galaxies: clusters: general – galaxies: clusters: individual: MACSJ1149.5+2223 – dark matter.

1 INTRODUCTION

The unprecedented data quality of the Hubble Frontier Fields (HFFs) programme[1] provides a good opportunity to study the mass distribution in the central region of merging clusters in detail. In addition, the HFF data are very useful to study the population of high-z galaxies and to discover new supernovae (or SNe hereafter). One of the SNe (SN Refsdal; Kelly et al. 2015) is one of the main subjects of this paper together with the mass distribution in the core of MACS1149.

The HFF images contain many tens of multiply lensed images that are not easily recognized, but require the guidance of a reliable model. This is partially due to the complexity of the clusters chosen for the HFF programme that maximizes the lensing signal. During

a major merger, the critical curves can be *stretched* between the mass components enhancing the critical area with elongated critical curves (Zitrin et al. 2013). This effect results in a relatively large sky area subjected to very large magnification and hence to the detection of unusually bright lensed galaxies. Galaxies as distant as $z \simeq 10$ have been identified through the HFF programme (Zitrin et al. 2014; Zheng et al. 2014; Oesch et al. 2014; Coe, Bradley & Zitrin 2015; Ishigaki et al. 2015) with the potential to reach $z \simeq 12$ given the spectral coverage of the HFF data.

The HFF programme may in fact be probing already the edge of the observable Universe at near-IR wavelength as so far there as yet no examples of galaxies beyond $z \simeq 10$ in the HFF data. This lack of higher redshift galaxies may be supported by the recently updated value for the mean redshift of reionization calculated from the inferred value of the optical depth, τ obtained by the *Planck* mission data for which a lower redshift (compared with previous estimations based on CMB data) of $z \simeq 8.8$ (for instantaneous or mean redshift of reionization) has been estimated, (Planck Collaboration XIII 2015). This has implications for the assumptions regarding

---

[*]E-mail: jdiego@ifca.unican.es
[†]Hubble Fellow.
[1] http://www.stsci.edu/hst/campaigns/frontier-fields/ (Lotz et al. 2014).

the spectral index of the ionizing radiation, and the extrapolation of the galaxy UV luminosity function to undetected luminosities together with the escape fraction of ionizing radiation from high-z galaxies. Despite these considerable uncertainties, consistency has been claimed between the recent low value of τ from Plank and the rough first measurements of the UV-selected luminosity density of $z > 9$ galaxies (Robertson et al. 2015; Bouwens et al. 2015). The initially claimed *steep decline* in the integrated UV luminosity density of galaxies at $z > 9$ would seem to empirically support this $z \sim 9$ epoch as marking the beginning of galaxy formation (Oesch et al. 2012, 2014) and interestingly this is not obviously reconciled with the many predictions made for λ cold dark matter (λCDM) with ever smaller galaxies naturally expected to higher redshift, in a scale free way, limited only by the relatively large Jeans scale for metal free star formation (McKee & Ostriker 2007; Barkana 2006). A lower redshift of galaxy formation is anticipated for CDM in the form of light bosons limited by a Jeans scale for the dark matter (DM) generated by quantum pressure of bosons in the ground state (Peebles 2000; Hu, Barkana & Gruzinov 2000). The first simulations of this form of CDM normalized to fit local galaxy DM cores predict the first galaxies at $z \simeq 12$ in a 30 Mpc volume (Schive, Chiueh & Broadhurst 2014) and hence this interpretation of CDM is more viable than heavy fermionic Weakly Interacting Massive Particless that are increasingly undetected in the laboratory. The HFF may provide considerably more clarity in deciding between these two very different interpretations of CDM by providing sufficient $z > 9$ galaxies with lower luminosities than field surveys, by virtue of the high levels of lens magnification.

Another important reason to study the HFF clusters is for the constraints that may be derived from the level of any self-interaction within the DM, as those clusters are caught in the act of collision. Although relaxed clusters seem to agree well with predictions from λCDM models (Newman et al. 2013), recent results on non-relaxed clusters show interesting deviations in the density profiles in the central regions when compared to predictions from standard λCDM. In particular, shallow profiles have been identified by several authors in HFF clusters and more in agreement with self-interacting DM expected for purely collisionless DM (Diego et al. 2015a,b; Lam et al. 2014). Other possible, and less exotic, interpretations may be related to projection effects, overlapping of cluster cores and uncertainties in the reconstruction of the central regions. More data and better hydrodynamical modelling of the HFF clusters may help resolve these questions. It is imperative therefore that free-form modelling of these lenses is achieved to reliably establish the density of background sources detected as a function of redshift.

In this paper, we explore the remarkable MACS1149($z = 0.544$) for which five very large well-resolved images of a spiral galaxy were recognized as multiple images (Zitrin & Broadhurst 2009; Smith et al. 2009) and subsequently explored more thoroughly with the Cluster Lensing And Supernova survey with Hubble (CLASH) programme (Rau, Vegetti & White 2014; Zitrin et al. 2015). These models demonstrate that the magnification is large over the full critical area of this cluster because of the flatness of the central density profile which lies close to the critical value for lensing in the central strong-lensing region and is hence optimal for creating high magnification. Indeed a very high redshift galaxy has been identified by the CLASH team (Zheng et al. 2012) at $z \simeq 9.6$, which has a high magnification. The power of this lens has led to its selection for the HFF programme in the search for more higher redshift lensed galaxies. The depth of the HFF data allows now many internal H II regions within five spiral galaxy images to be identified and matched between the counter-images. Moreover, the distribution of the multiple counter-images map the central region in a semicontinuous fashion from distances $R = 13.12$ arcsec (or $R = 84.62$ kpc) to only $R = 1.26$ arcsec (or $R = 8.12$ kpc) from the centre of the dominant Brightest Cluster Galaxy (BCG). In addition, an SN is observed multiply lensed four times around a cluster member galaxy (Kelly et al. 2015). This SN is observed in only one of the counter-images to date. The corresponding SN event in the other counter-images has either occurred in the past of will happen in the future. Time delays between the different counter-images have been computed by different authors but with estimates varying in general by several years between the different authors (Oguri 2015; Sharon & Johnson 2015; Kelly et al. 2015). The time delay between the counter-images depends on the lens model, position of the background source and cosmology (in particular the Hubble constant). Having an accurate time delay for this SN will be useful to plan an observing campaign of the *future* SN. This will offer the rare opportunity to study the SN from the very early phases, providing also a test of competing lensing models and a consistency check of cosmological models.

Here we implement an enhancement to our free-form method, WSLAP+ (Diego et al. 2005, 2007; Sendra et al. 2014), which is largely motivated by the uniqueness of the particularly large lensed images generated by MACSJ1149 ($z = 0.544$) and we calculate the corresponding time delays for the SN event. The paper is organized as follows. We describe the Hubble data in Section 2. The X-ray data are described in Section 3. The lensing data are described in Section 4. In Section 5, we give a brief description of the reconstruction method with the new improvements that are applied to the data for the first time in this work. Section 5.2 describes six different scenarios that are assumed to reconstruct the lens and to study the uncertainties and variability in the solutions. Section 6 presents the results of the lensing analysis, focusing on the reproducibility of system 1, the two-dimensional mass distribution, the projected mass profile and the time delays for the Refsdal SN. We conclude in Section 7.

Throughout the paper, we assume a cosmological model with $\Omega_M = 0.3$, $\Lambda = 0.7$ and $h = 70$ km s^{-1}Mpc^{-1}. For this model, 1 arcsec equals 6.45 kpc at the distance of the cluster.

2 HFF DATA

In this paper, we use public imaging data obtained from the Advanced Camera for Surveys (ACS) (filters: F435W, F606W and F814W) and the WFC3 (F105W, F125W, F140W and F160W), retrieved from the Mikulski Archive for Space Telescope. The data used in this paper consist of $\approx 1/3$ of the data to be collected as part of the HFF programme. Part of the data comes from CLASH (Postman et al. 2012). This release includes the first 70 orbits of observations of MACS1149 from the Frontier Fields programme ID 13504 (PI. J. Lotz) but also including archival ACS and WFC3/IR data from programmes 13790 (PI. S. Rodney) and 14041 (PI. P. Kelly). In the IR bands, we use the background corrected images, corrected for a time-dependent increase in the background sky level (see for instance Koekemoer et al. 2013). From the original files, we produce two sets of colour images combining the optical and IR bands. The first set is based on the raw data while in the second set we apply a low-pass filter to reduce the diffuse emission from member galaxies and a high-pass filter to increase the signal-to-noise ratio of small compact faint objects. The second set is particularly useful to match colours in objects that lie behind a luminous member galaxy.
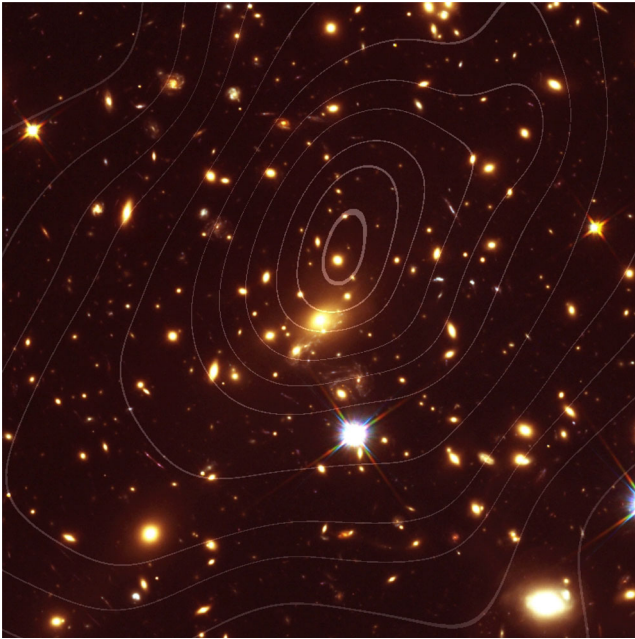
**Figure 1.** MACS1149 as seen by *HST* with *Chandra* contours overlaid on top. The field of view is 1.6 arcmin.

3 X-RAY DATA

To explore the dynamical state of this cluster, we produce an X-ray image using recent public *Chandra* data on this cluster. In particular, we use data with the following Obs IDs, 1656, 3589, 16238, 16239, 17595, 17596, 16306, 16582 (PIs. Vaspeybroeck, Jones, Murray) totalling 363.4 ks. The X-ray data are smoothed using the code ASMOOTH (Ebeling, White & Rangarajan 2006). The smoothed X-ray map is compared with the distribution of galaxies in Fig. 1.

A significant offset is observed between the peak of the X-ray emission and the BCG indicating that this cluster shows the effect of collision. The X-ray emission is elongated in the diagonal direction and, as discussed later, the same elongation is found in the distribution of matter although the peak of the mass distribution is also found to be offset with respect to the peak of the X-rays and more in agreement with the position of the BCG.

4 LENSING DATA

For the lensing data, we adopt the previous multiple-image system identifications from CLASH data (Zitrin et al. 2015) from which we also adopt his numbering system except for systems 2 and 3 that are swapped like in Smith et al. (2009). In particular, we use the reliable systems 1–6 and 8. For systems 5 and 6, we use only two of the counter-images as the remaining third counter-image is not regarded as reliable (various candidates are consistent with being the counter-part of the third images, 5.3 and 6.3). Further HFF data will soon help clarify these and uncover other systems. Systems 1–3 have spectroscopic redshifts that we take from the compilation of Zitrin et al. (2015) and were originally measured by Smith et al. (2009). The redshifts of systems 4–6 and 8 are matched to the redshifts preferred by the lens models (see below) which constrain the position of the critical curve. For these four systems, the redshifts preferred by our lens model are between 10 and 30 per cent higher than the inferred redshifts (also from a lens model) derived by Zitrin et al. (2015). We should note that the redshifts for systems 4–6 and 8 may differ from estimates used also by other authors. This may
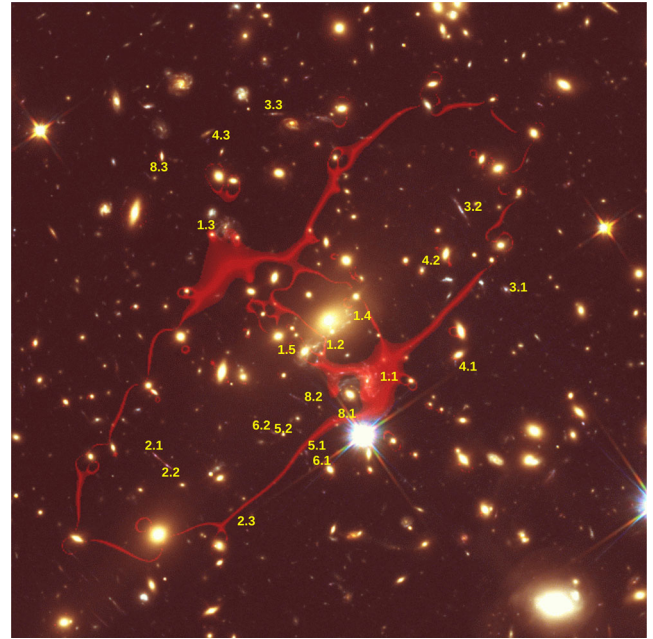
Figure 2. MACS1149 with a typical critical curve ($z_s = 3$) for one of our models (case 5, see text). The images used in the reconstruction are marked with yellow IDs. The field of view is 1.6 arcmin.

result in differences in the derived mass model. More specifically, for systems 1–6 and 8, we adopt the following redshifts: 1.491, 1.894, 2.497, 2.5, 1.9, 1.9 and 2.5, respectively. The systems are shown in Fig. 2. For comparison purposes, we also show the critical curve for one of our models for a source at redshift $z = 3$.

In addition to the position of these lensed systems, for some of them we use the position of knots readily identified in the different counter-images thanks to the depth of the data (see Fig. 3). The large image 1.1 (in the notation of Zitrin & Broadhurst 2009) is the largest, most magnified image of system 1 (and displays the four SN images) with many internal features that we label in Fig. 3. Lensed systems 3 and 8 are also morphologically resolved allowing us to identify a few individual knots and these are also included in our new reconstruction algorithm. In order to take full advantage of the resolved geometry of system 1 (and to a lesser extent of systems 3 and 8), we introduce two enhancements to our code that are described in the next section.

## 5 LENSING RECONSTRUCTION AND IMPROVEMENTS TO THE CODE

We use the method, WSLAP+, that we have been developing to perform the lensing mass reconstruction with the lensed systems and internal features described above. The reader can find the details of the method in our previous papers (Diego et al. 2005, 2007; Sendra et al. 2014). Here we give a brief summary of the most essential elements.

Given the standard lens equation,

$$\beta = \theta - \alpha(\theta, \Sigma), \qquad (1)$$

where θ is the observed position of the source, α is the deflection angle, $\Sigma(\theta)$ is the surface mass density of the cluster at the position θ and β is the position of the background source. Both the strong-lensing and weak-lensing observables can be expressed in terms of
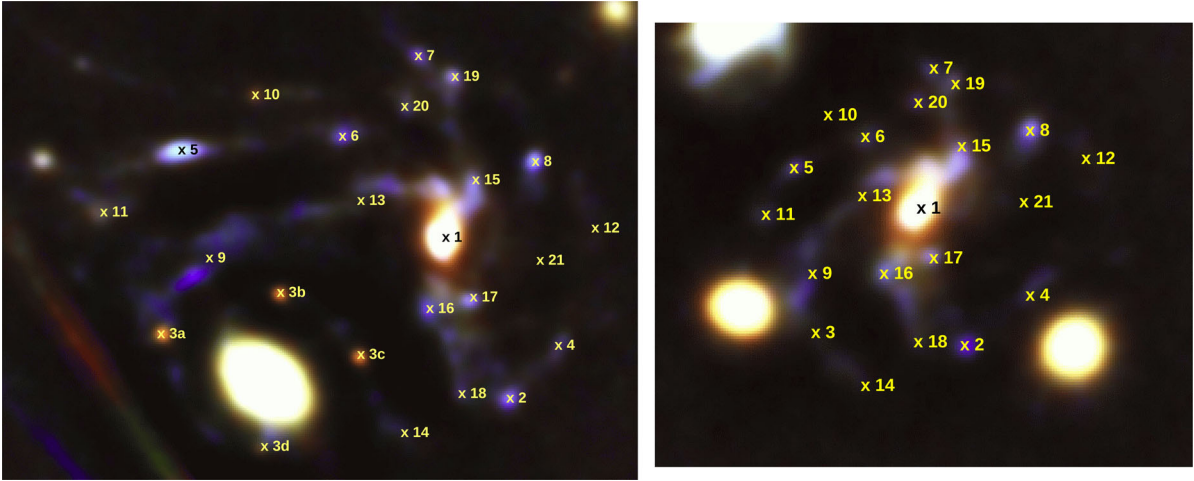
Figure 3. Knots for system 1 used to do the mass reconstruction. Only two of the counter-images of system 1 are represented here.

derivatives of the lensing potential.

$$\psi(\theta) = \frac{4\,G\,D_l D_{ls}}{c^2\,D_s} \int d^2\theta' \Sigma(\theta') ln(|\theta - \theta'|), \qquad (2)$$

where D_l, D_s and D_{ls} are the angular diameter distances to the lens, to the source and from the lens to the source, respectively. The unknowns of the lensing problem are in general the surface mass density and the positions of the background sources in the source plane. The surface mass density is described by the combination of two components:

(i) A soft (or diffuse) component that is parametrized as a superposition of Gaussians on a grid of constant width (regular grid) or varying width (adaptive grid).

(ii) A compact component that accounts for the mass associated with the individual haloes (galaxies) in the cluster. This component is modelled either as Navarro Frenk and White (NFW) profiles with a mass proportional to the light of each galaxy or adopting directly the light profile (in one of the IR bands).

The compact component is usually divided in independent layers, each one containing one or several cluster members. The separation in different layers allows us to constrain the mass associated to special haloes (like the ones from giant elliptical galaxies) independently from more ordinary galaxies. This is useful in the case where the light-to-mass ratio may be different, like for instance in the BCG.

As shown in Diego et al. (2005, 2007), the strong- and weak-lensing problem can be expressed as a system of linear equations that can be represented in a compact form,

$$\Theta = \Gamma X, \qquad (3)$$

where the measured strong-lensing observables (and weak lensing if available) are contained in the array Θ of dimension $N_\Theta = 2N_{SL}$, the unknown surface mass density and source positions are in the array X of dimension $N_X = N_c + N_g + 2N_s$ and the matrix Γ is known (for a given grid configuration and fiducial galaxy deflection field) and has dimension $N_\Theta \times N_X$. N_{SL} is the number of strong-lensing observables (each one contributing with two constraints, x and y), N_c is the number of grid points (or cells) that we use to divide the field of view. Each grid point contains a Gaussian function. The width of the Gaussians is chosen in such a way that two neighbouring grid points with the same amplitude produce a horizontal plateau in between the two overlapping Gaussians. N_g

is the number of deflection fields (from cluster members) that we consider. In this work, we set N_g equal to 3. The first deflection field contains the BCG galaxy, the second contains a prominent elliptical galaxy near the image 1.2 and the third deflection field contains the remaining galaxies ($N = 121$) from the cluster that are selected from the red sequence (totalling 123 galaxies between the three layers). Dividing the cluster galaxies in three layers allows us to independently fit the mass of the two giant ellipticals from the other galaxies. The particular configuration of the galaxies in the three layers is shown in Fig. 10. N_s is the number of background sources (each contributes with two unknowns, β_x and β_y) which in our particular case is $N_s = 7$. The solution is found after minimizing a quadratic function that estimates the solution of the system of equations (3). For this minimization, we use a quadratic algorithm which is optimized for solutions with the constraint that the solution, X, must be positive. Since the vector X contains the grid masses, the renormalization factors for the galaxy deflection field and the background source positions, and all these quantities are always positive (the zero of the source positions is defined in the bottom-left corner of the field of view), imposing $X > 0$ helps in constraining the space of meaningful solutions. The condition $X > 0$ also helps in regularising the solution as it avoids large negative and positive contiguous fluctuations. The quadratic algorithm convergence is fast (few minutes) on a desktop allowing for multiple solutions to be explored on a relatively short time. Different solutions can be obtained after modifying the starting point (or grid configuration) in the optimization. A detailed discussion of the quadratic algorithm can be found in Diego et al. (2005). A recent discussion about its convergence and performance can be found in Sendra et al. (2014).

5.1 New enhancements

Two improvements are implemented that resolve some of the issues found in the previous version of the code. One of the problems of the original code was a systematic bias introduced in the reconstructed solution when using a multiresolution grid. This bias was the consequence of sharp changes in resolution between neighbouring cells (or Gaussians). The difference in size between two cells of different resolutions was a factor 2^n which introduced spurious artefacts in the space dividing two resolutions. We have mitigated this problem by introducing a more gradual change between neighbouring cells. An example of the new scheme for the multiresolution grid is shown
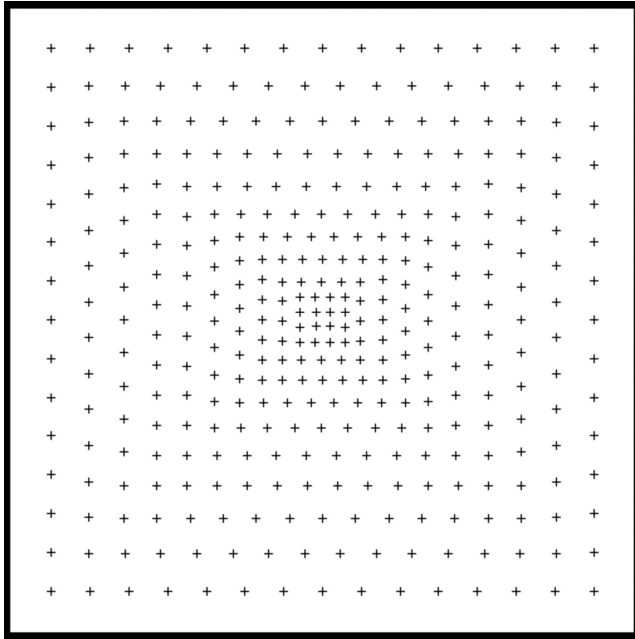
Figure 4. Example of a multiresolution grid (352 grid points). The peaks of the individual Gaussians are located at the positions of the crosses. The width of the Gaussians is adjusted to guarantee a smooth constant distribution when the amplitudes are equal. This distribution is suited to the increasing strong-lensing data density towards the centre.

in Fig. 4. The use of the multiresolution grid with increased resolution around the BCG has the advantage of allowing for a more complex mass distribution in the central region where the density of lensed image constraints is higher and in particular it allows for a better and more flexible way of parametrizing the elongation of the DM halo in the central region. As a general rule, when using the new multiresolution grid we always increase the density of grid points towards the centre (BCG). The difference in the width of the Gaussians between two consecutive grid points is a constant fraction that can be changed depending on the desired degree of freedom.

A second improvement is related with the original assumption that the sources are very compact. This assumption is normally a good approximation but in cases like system 1, this assumption would result in unphysical solutions that predict a very small source for system 1 in the source plane. This pathological problem was extensively discussed in our earlier work (Diego et al. 2005, 2007; Ponente & Diego 2011) and the solutions derived from it were referred to as the *point source* solution. Information related to the shape of the galaxies in the source plane can be easily integrated in the algorithm. Based on a preliminary solution that avoids this pathological behaviour, it is possible to produce a good guess for the shape and size of the galaxy in the source plane. This information on the expected shape (and size) of the source can be incorporated in the algorithm as additional constraints. The minimization process then converges to a solution that is stable and does not produce unphysical solutions (like the *point source* solution discussed in our earlier work). A similar behaviour was observed when introducing the deflection field from the member galaxies as part of the lens model as they act as an *anchor* for the solutions, better constraining the range of possible solutions. A future improvement of the code will include a penalty function for those models that predict images (knots) at positions that are not observed. This approach was already

initially explored in Diego et al. (2005) with promising results (and referred to as the *null space*).

5.2 Models

To account for uncertainties and variability in the solutions, we explore a range of cases where we change the assumptions for the two main components of our method: the member galaxies and the grid definition. In particular, we consider six types of models (or cases) described briefly below.

(i) Case 1: We use a standard grid of $16 \times 16 = 256$ cells in our field of view. Each member galaxy is assigned an NFW profile where its total mass is taken proportional to its luminosity in the 814W filter band. The scale radius of the NFW is derived from the mass assuming a scaling $M^{1/3}$. The concentration parameter is fixed to $C = 8$.

(ii) Case 2: Like case 1 but instead of a uniform regular grid we use a multiresolution grid with 280 cells similar to the one shown in Fig. 4.

(iii) Case 3: Like case 2 but instead of a multiresolution grid with 280 cells we increase the resolution and use a grid with 576 cells.

(iv) Case 4: Like case 1 but we divide the scale radius by a factor 2 making the galaxies more compact.

(v) Case 5: Like case 2 but we divide the scale radius by a factor 2 making the galaxies more compact.

(vi) Case 6: Like case 3 but we divide the scale radius by a factor 2 making the galaxies more compact.

In addition to these cases, we briefly consider the equivalent of case 1 but in our previous implementation of the code where no information about the spatial extent of system 1 is used and the galaxy in the source plane is assumed to be very compact. We refer to this case as the *singular* case and would correspond to the solution obtained with our previous version of the code in the situation of maximum convergence (referred as *point source* solution in Diego et al. 2005; Sendra et al. 2014). In all cases, we assume three deflection fields for the galaxies as described in the previous section. Most of the galaxies are contained in one deflection field. The BCG and the elliptical next to image 1.2 are treated as independent deflection fields and their masses are rescaled by the algorithm in the minimization process. For the remaining cluster members, their masses are also rescaled but all by the same factor.

6 RESULTS

For each one of the six cases discussed in Section 5.2 we derive a solution. The minimization is stopped once the solution has converged to a stable point (typically between 50 000 and 150 000 iterations). In our earlier implementation of the code, such a large number of iterations would have produced solutions that predict unphysically small sources. This case is explicitly shown in Fig. 5 (singular case), a situation that is avoided in our new implementation once the additional information regarding the source shape and size (for well resolved and extended arcs) is incorporated. We use the same number of iterations to derive the six solutions. A first comparison between the different solutions is made by contrasting the reconstructed shape of the original (delensed) galaxy of system 1 in the source plane. Fig. 5 shows the predicted shape of the galaxy of system 1 in the source plane based on image 1.3. We find that changing the scale radius of the member galaxies has no significant effect on the deflection field around image 1.3. This is not surprising as 1.3 lies in a region of the cluster with no major
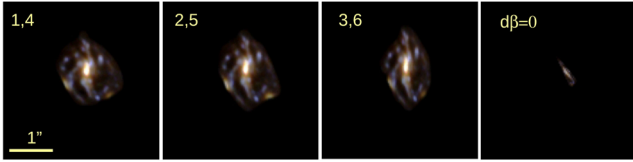
Figure 5. Delensed image 1.3 for the six models. Only the cases for models 1–3 are shown. Cases 4–6 are virtually indistinguishable from 1–3, respectively. For comparison, the panel on the right end shows the case for the same number of iterations but without a constrain on the size of the source (or singular case). The number indicates the case discussed in Section 5.2. All figures have the same scale.
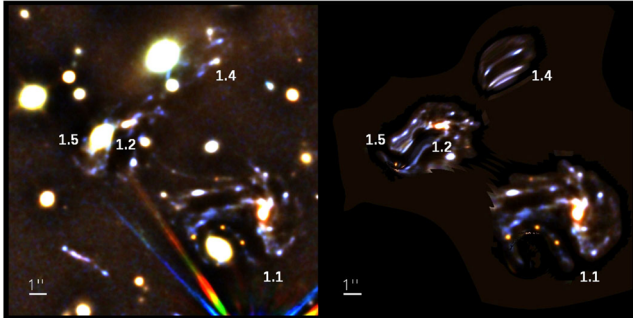
Figure 6. Original (left-hand panel) versus model-predicted (right-hand panel) counter-images for system 1 (the model corresponds to case 5). The largest counter-image 1.1 (bottom right of the left-hand panel) is used to predict the other counter-images. The centre and field of view are the same in both panels. Note how the reproduction of 1.4 is still affected by significant errors probably related to imperfect modelling of the BCG and neighbouring galaxy at ≈1 arcsec south from the BCG.

member galaxies. Consequently, the delensed images of cases 1–3 are virtually indistinguishable from those of cases 4–6, respectively. Comparing the different cases in Fig. 5, increasing the resolution of the grid seems to result in an elongation of the galaxy in the vertical direction. The right-hand panel in the same figure shows the corresponding solution for the case where no prior information about the shape of the galaxy is included and the algorithm reconstructs an unphysically small galaxy in the source plane. This is the solution that would have been derived with a very large number of iterations in our previous version of the code. Although Fig. 5 represents only the delensed version of image 1.3, using 1.1 renders similar results. The other counter-images (1.2, 1.4 and 1.5) produce more distorted and/or partial reconstructions of the source.

A further assessment of the quality of the solution can be tested by comparing the observed and predicted counter-images in the image plane. We focus on system 1 as this is the most interesting one in terms of complexity and also due to its proximity to the centre of the cluster. Fig. 6 shows the challenging cases of images 1.2, 1.4 and 1.5 (for the model corresponding to case 5 described in the previous section). For this example, we use 1.1 as a template for the source that is delensed and relensed by our lens model to predict the other counter-images. The agreement between the observed and predicted images is in general very good with typical distances between observed and predicted features smaller than 1 arcsec.

The prediction for all six models is shown in Fig. 7. In general, all models reproduce the observed image reasonably well. Image 1.4 is the most challenging and some significant deviations can be appreciated in some of the models. In particular, models 1, 3, 4 and 6 predict an additional counter-image for the nucleus that is not observed in the current data although it cannot be ruled out

that the counter-image for the nucleus is lost in contrast with the central glare of the BCG. The upcoming deeper optical data from the HFF programme (specially the UV band where the BCG will be relatively faint) will certainly help in testing for the existence of this possible additional image of the bulge of system 1.[2] Knot number 8 (see Fig. 3) in image 1.2 seems to be reproduced better (closer to the BCG) in the case of the regular grid with the more extended (i.e. larger scale radius) galaxies (case 1) suggesting that the mass distribution stretches and flattens in the direction connecting the BCG with the elliptical galaxy next to 1.2. Regarding the SN, no counter-image of the SN is expected around the BCG as shown in Fig. 12 below.

The result for the counter-image 1.3 is shown in Fig. 8 for case 5. As in the previous case, 1.1 is used to delens and relens the galaxy. The agreement is again very good, with the exception of the SN that appears in four locations while a perfect model would predict only one location. This is due, in part, to the fact that the elliptical in between the SN is modelled as a spherical halo. We should not that the observed image 1.3 does not show the SN as it probably appeared at this position several years ago and was missed by the observations while the prediction above is based on an image that does contain the SN.

Future improvements to the lens model will include a halo based on the elongation of the luminous matter (Chen, in preparation). The predicted images 1.3 for the six models are shown in Fig. 9. All images are centred on the same position as the left-hand panel of Fig. 8 and have the same scale. The agreement for all models is also excellent, with some models like cases 3 and 6 (high-resolution grid) showing some distortion in the northern part of the galaxy. Cases 1 and 4 (regular grid) show an elongation in the diagonal direction. These distortions may be connected with the fact that the spiral galaxy in the north-east (possibly a cluster member) was not included in our set of cluster members as it is not included in the red sequence. Due to the proximity of this spiral galaxy to image 1.3, a small distortion in the deflection field might be expected. The predictions from cases 2 and 5 (intermediate resolution grid) seem to best reproduce image 1.3.

The solutions show some sensitivity to the redshifts of systems with photo-z in particular to images 4.3 and 8.3. Excluding images 4.3 and 8.3 from our analysis produces more smooth solutions and a rounder critical curve. These solutions (without 4.3 and 8.3) reproduce better the image pairs 4.1, 4.2 and 8.1, 8.2 with a lower redshift. Imminent new optical data from the HFF should improve photo-z estimations and provide new systems that will help constrain the solution better. This will be explored in a future paper (Treu et al. 2015).

6.1 Mass profile and mass distribution

The two-dimensional distribution of the soft component (grid) for the mass is shown in Fig. 10 and is compared with the position (and shape) of the input galaxies and with the X-ray emission from *Chandra*. A few interesting conclusions can be derived from this plot. First, the peak of the soft component lies close to the position of the BCG. The small misalignment may be natural since the BCG may not be at rest with respect to the projected centre of mass or this may be a consequence of our assumption of a spherical halo for the BCG while clearly the *Hubble Space Telescope* (*HST*) data

---

[2] The new *HST* UV data do not show any counter-image of the bulge in 1.4.
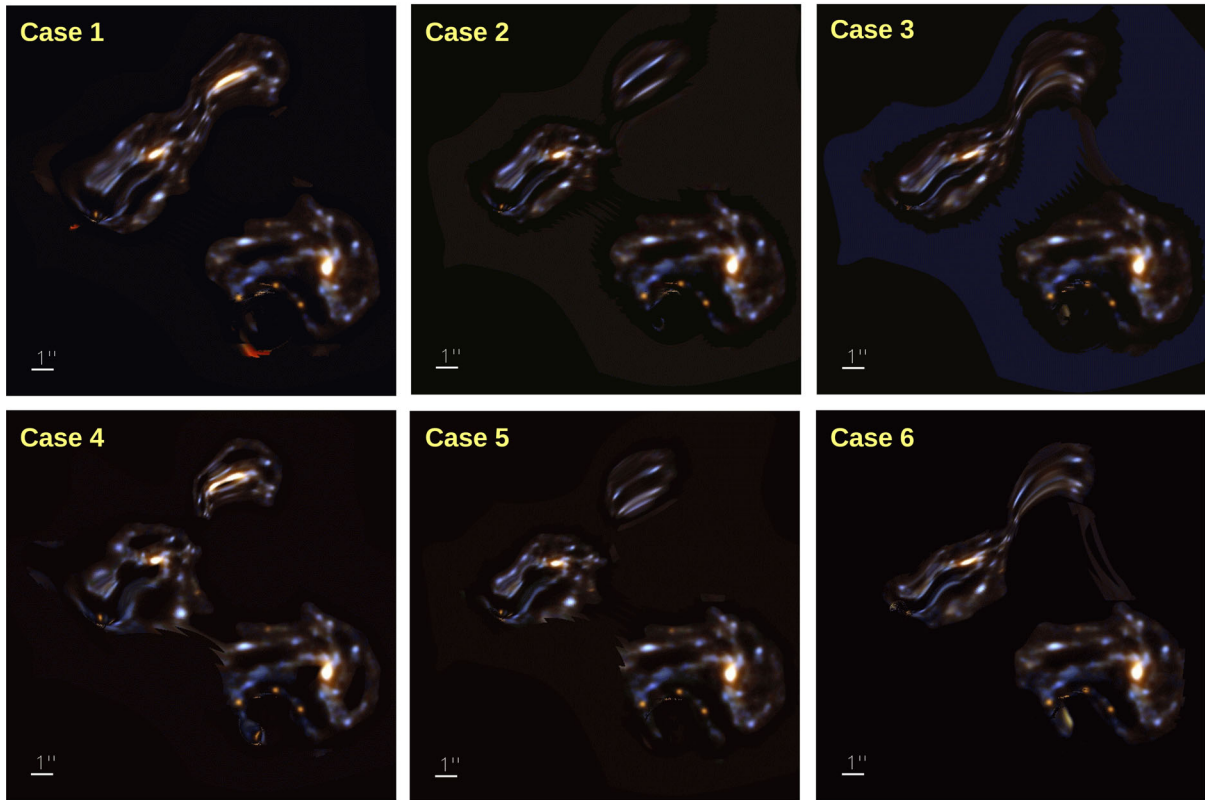
Figure 7. Predicted images using the delensed 1.1 as a template of the source for the six different cases discussed in Section 5.2. Note how models 1, 3, 4 and 6 predict and extra counter-image for the nucleus that is not observed. The scale and centre of the images are the same as the left-hand panel of Fig. 6.

suggest an elongation for this halo. The location of the peak and the elongation of the soft component around the BCG seems to correct for this wrong assumption by adding an elongation to the global mass distribution (or deflection field). Interestingly, this elongation points in the direction of the X-ray peak that is offset from the BCG by ≈ 50 kpc. Also, in the direction of the X-ray peak there is another prominent member galaxy that was not fitted independently in our model. Better constraints around this massive galaxy derived from the imminent new HFF optical data will help constrain this galaxy in an independent way. The offset between the X-ray and mass peaks confirms the disturbed nature of this cluster.

The mass profiles for the six models are shown in Fig. 11. A general good agreement is found between the six models. For comparison, we show the profile derived recently by Zitrin et al. (2015) from the CLASH survey. A small shift is observed between the parametric solution of Zitrin et al. (2015) and our free-form solution. The origin of this small discrepancy may be the fact that for systems 4 and 8 we use a redshift that is different than the one assumed in Zitrin et al. (2015). In contrast with our previous work on HFF clusters (A2744, MACS0516 and MACS0717), no plateau is observed in the profile beyond the outer radius of the central galaxy. We find a good agreement between our derived profile and a low concentration NFW profile expected for massive clusters. According to results from simulations (Meneghetti et al. 2014), and recent observations on clusters (Merten et al. 2015), massive galaxy clusters are well reproduced by NFW profiles with relatively low values of the concentration parameter, $C \approx 3$–4, with somewhat larger values are derived for well defined relaxed clusters from the CLASH programme (Umetsu et al. 2014; Zitrin et al. 2015). In the particular case of MACS1149, we find that an NFW profile
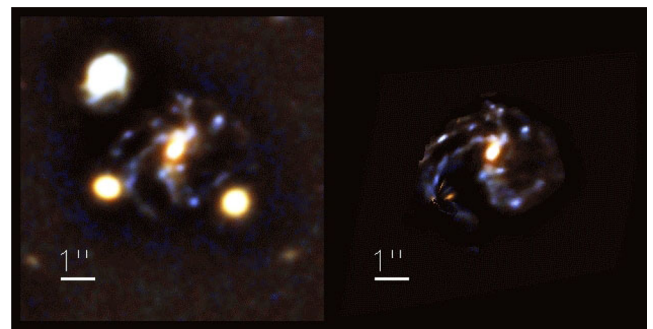

Figure 8. Like in Fig. 6 but for the counter-image 1.3 in the north and for case 5. The two *twin* elliptical galaxies in the south are included in our model. The blue spiral galaxy in the north-east is not included in our model and may still play a non-negligible role by stretching the deflection field in the direction north-west.

with a concentration $C = 3$ produces a good match to the observed projected profile, consistent with the dynamical state of this cluster which from our comparison of the gas and DM distribution (Fig. 10) is evidently not suffering a first core passage of a major merger, but is not yet well relaxed.

6.2 Time delays

Here we use our free-form models to obtain the 2D-time delay surface (and uncertainty) for this cluster. Image 1.1 hosts a quadruply lensed SN (and named in honour of Refsdal for his pioneering interest in this regard; Refsdal 1964). Several authors have predicted
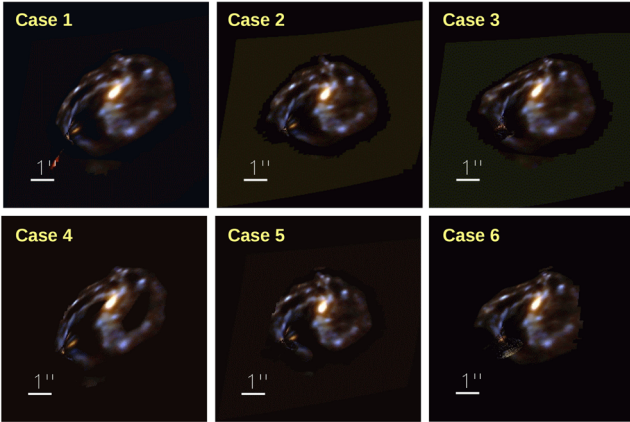
**Figure 9.** Like Fig. 7 but for the predicted counter-image 1.3 in the northern part.
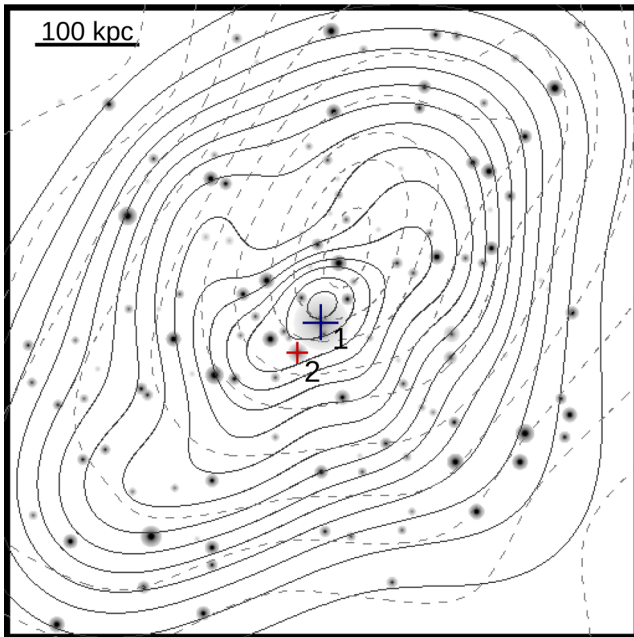
Figure 10. Contours of the grid component of the mass distribution for case 5 (solid lines) compared with the X-ray emission as seen by *Chandra* (dashed lines). The input galaxies used in our model (for cases 4–6) are shown for comparison. The galaxies defining layers 1 and 2 are marked with a big blue and small red cross, respectively. The remaining galaxies form the layer 3 in our model.

the time delays between the four SN counter-images in 1.1 and the predicted position of the SN in images 1.2 and 1.3. Oguri (2015) predicts the SN in 1.3 appeared 17 yr ago while one in 1.2 will appear in 1–3 yr. In Sharon & Johnson (2015), the authors predict that the SN in 1.2 will appear in ≈ 0.65 yr (around early 2015 July with ≈ 1 month uncertainty) after the SN is observed in 1.1. The same model predicts the SN in 1.3 occurred ≈ 11.6 yr before the SN in 1.1 was observed (with ≈ 1 yr uncertainty). The suite of models produced by the method of Zitrin & Broadhurst (2009) and Zitrin et al. (2015) as presented in Kelly et al. (2015) also predicts time delays consistent with these predictions although with larger error bars in part due to the exploration of a wider range of models and the addition of uncertainties in the photometric redshifts. In contrast, we restrict the computation of our uncertainties to just the six
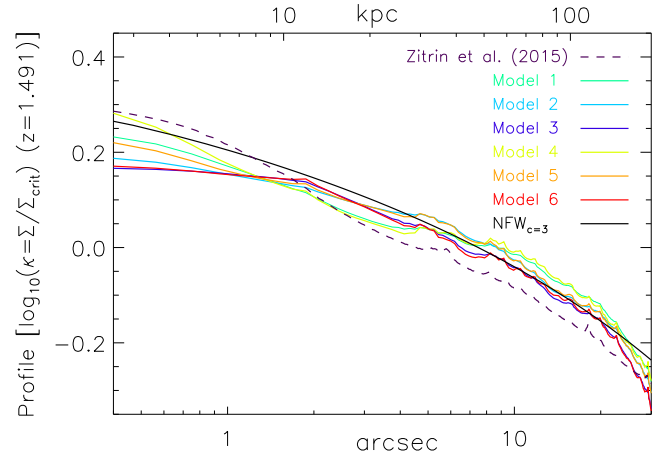
Figure 11. Mass profile in terms of the critical surface mass density (computed at $z = 1.491$) for the six solutions obtained with the regular grid and with the multiresolution grids. The dashed line is the recent estimate from Zitrin et al. (2015). The solid black line is a projected NFW profile with concentration $C = 3$ and $R_{200} = 5$ Mpc.
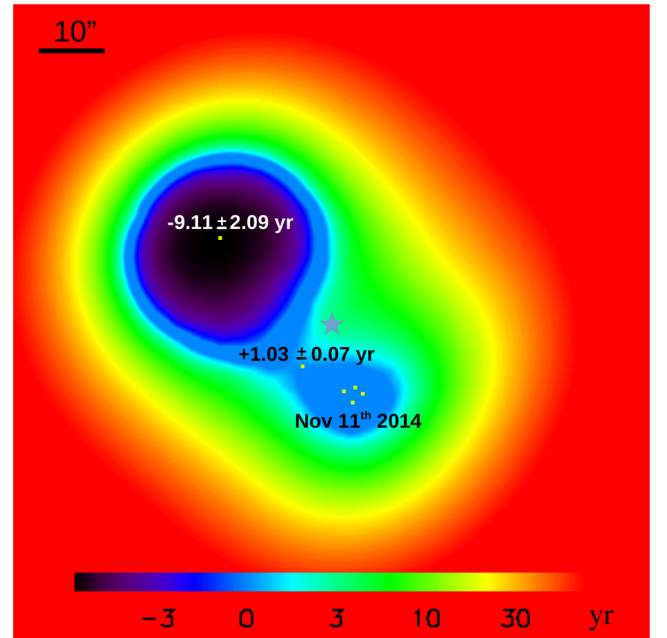
Figure 12. Time delay surface computed with respect to the quadruply lensed SN. The yellow dots mark the location of the four SN images and the predicted positions of the SN in two counter-images. The time delays for the additional counter-images lie ≈ 9 yr in the past for the counter-image 1.3 and ≈ 1 yr in the future for the counter-image 1.2. The star marks the position of the cluster BCG.

models presented above and no errors are adopted for the photometric redshifts so our error bar is likely to be underestimated.

We compute time delays from our six models and estimate the mean and dispersion from these six models. The time delay is defined as

$$t(\theta) = \frac{1 + z_{\mathrm{d}}}{c} \frac{D_{\mathrm{d}} D_{\mathrm{s}}}{D_{\mathrm{ds}}} \left[\frac{1}{2}(\theta - \beta)^2 - \psi(\theta) \right]. \quad (4)$$

Fig. 12 shows the average time delay from our models. The counter-image in 1.2. lies in the future by approximately 1 yr with respect to the observed SN. If the model prediction is correct, the

SN should appear again by the end of 2015. The counter-image of the SN at image 1.3 is predicted to have occurred approximately 9 yr ago. These predictions are similar to those derived by Sharon & Johnson (2015). Also. a visual comparison of our Fig. 12 with the bottom-left panel of fig. 4 in Sharon & Johnson (2015) reveals a similar structure in the two-dimensional distribution of the time delay. The agreement between our free-form prediction and their parametric predictions favours strongly a window around 2015 July–December to observe the SN in image 1.2 at RA = 11:49:36.025, Dec.=+22:23:48.11 (J2000).

A measurement of the time delay in the near future can be used to impose tight constraints in the lens model. Small differences between models result in small changes in the balance between the terms $(\theta - \beta)^2$ and $\psi(\theta)$ which are later magnified by the factor $\frac{1+z_d}{c}\frac{D_d D_s}{D_{ds}}$. This factor typically takes values of ∼1 Gyr. A discrepancy in the time delay prediction of 1 yr between models is possible with small changes of order 10^{-9} in the difference shown in brackets in equation (4). Note that these models do not predict the time of explosion of the SN, which is estimated empirically to be about 3 weeks prior to the 2014 November NIR observations in which it was discovered (Kelly et al. 2015), so that when predicting the date of the future SN explosion anticipated for image 1.2, we must subtract off about 3 weeks. We estimate then that the SN will reappear around November 1st, and with an uncertainty of 25 d. If the SN is in fact observed in the near future in image 1.2, this observation could be used to improve the constraints in the lens model and perhaps even cosmological parameters like the Hubble constant. For the current paper, we have adopted the value $h = 0.7$ for the Hubble constant. While the strong-lensing constraints are not sensitive to h (due to the degeneracy in h between the geometric factor and the cluster mass), the time delay exhibits a different dependence with the Hubble constant. Accurate estimations of the mass based on strong-lensing constraints can be used to derive precise predictions of the time delay that scale as h^{-1} and when contrasted with measurements of these time delays, derive a constraint on h (Oguri 2007).

In the particular case of WSLAP+, time delay constraints can be easily incorporated if one makes the approximation that the change in position of the background source is small (in relation to the typical deflection angles) when time delays constraints are incorporated in the reconstruction. In this case, the unknown variable β in the quadratic term $(\theta - \beta)^2$ can be expressed as a fixed term, β_0, plus a small perturbation, $\delta\beta$.

$$
\begin{aligned}
(\theta - \beta)^2 &= (\theta - (\beta_0 + \delta\beta))^2 \\
&= (\theta - \beta_0)^2 + \delta\beta^2 - 2\theta \times \delta\beta \\
&\approx C - 2\theta \times \delta\beta,
\end{aligned}
\tag{5}
$$

where β_0 is the source position as inferred from the arc positions in the standard strong-lensing analysis, $\delta\beta$ is the offset (with respect to β_0) of the new source position when time delays are included, C is a known variable (constant) that can be pre-computed and we make the approximation that the term $\delta\beta^2$ is much smaller than the other terms so it can be neglected. This assumption is good if in fact the offset between the new source position and that inferred from the strong-lensing constraints is indeed small when compared with the typical deflection angles. When computing $\delta\beta$ for our six solutions, we find that the relative change between the six models is indeed very small (less than 1 arcsec). Hence, if time delays are able to discern between different models (like the ones used in this work), the approximation that $\delta\beta^2$ is very small is valid. Under this approximation, equation (4) can be linearized in the unknown

variables (mass and source position) and solved using the same fast optimization algorithm (system of linear equations). Fixing β_0 requires solving the problem in an iterative way where each time the value of β_0 is updated. The convergence of the algorithm when time delays are included will be tested in a future work.

7 CONCLUSIONS

We apply our improved lensing reconstruction algorithm to the HFF cluster MACS1149. The new enhancements in the code to incorporate the internal structure of the large spiral galaxy images, in which the Refsdal SN was found, result in solutions that are more stable and precise. The increased precision in the solutions allows us to reproduce the observed images with unprecedented detail for a free-form method. Our best-fitting mass distribution shows a somewhat disturbed but single cluster well fitted radially by an NFW profile with a low concentration value, $C = 3$, typical for large unrelaxed clusters (Neto et al. 2007). We confirm an offset between the X-ray and mass maxima, that is similar to the offset observed between the centre of the cluster BCG and the X-ray peak. The peak of the diffuse mass distribution extends towards the position of the X-ray peak suggesting that the lensing data may be sensitive to the X-ray plasma, a possibility already suggested by our earlier HFF work on A2744 and MACS0416 (Lam et al. 2014; Diego et al. 2015b).

Our improved model allows us to compute precise time delays for the observed Refsdal SN. Our results are in agreement with previous estimates and places the future occurrence of the SN somewhere between early 2015 October and early 2016 January (assuming a value for the Hubble constant of $h = 0.7$). A significant deviation from this prediction will result in changes in the lens model and/or the cosmological model (in particular h). The inclusion of a future observation of this time delay can be easily incorporated in our reconstruction algorithm and will be exploited in future work. The planned deep optical observations of this cluster as part of the ongoing HFF will reveal new multiply lensed images that will help in constraining better this cluster, in particular the haloes of the perturbing central member galaxies including the BCG, for which currently the data are still very ambiguous.

---

[3] ivo://ADS/Sa.CXO#obs/1656
[4] ivo://ADS/Sa.CXO#obs/3589
[5] ivo://ADS/Sa.CXO#obs/16238
[6] ivo://ADS/Sa.CXO#obs/16239
[7] ivo://ADS/Sa.CXO#obs/17595
[8] ivo://ADS/Sa.CXO#obs/17596
[9] ivo://ADS/Sa.CXO#obs/16306
[10] ivo://ADS/Sa.CXO#obs/16582

REFERENCES

Barkana R., 2006, Science, 313, 931
Bouwens R. J., Illingworth G. D., Oesch P. A., Caruana J., Holwerda B., Smit R., Wilkins S., 2015, ApJ, 811, 140
Coe D., Bradley L., Zitrin A., 2015, ApJ, 800, 84
Diego J. M., Protopapas P., Sandvik H. B., Tegmark M., 2005, MNRAS, 360, 477
Diego J. M., Tegmark M., Protopapas P., Sandvik H. B., 2007, MNRAS, 375, 958
Diego J. M., Broadhurst T., Zitrin A., Lam D., Lim J., Ford H. C., Zheng W., 2015a, MNRAS, 451, 3920
Diego J. M., Broadhurst T., Molnar S. M., Lam D., Lim J., 2015b, MNRAS, 447, 3130
Ebeling H., White D. A., Rangarajan F. V. N., 2006, MNRAS, 368, 65
Hu W., Barkana R., Gruzinov A., 2000, Phys. Rev. Lett., 85, 1158
Ishigaki M., Kawamata R., Ouchi M., Oguri M., Shimasaku K., Ono Y., 2015, ApJ, 799, 12
Kelly P. L. et al., 2015, Science, 347, 1123
Koekemoer A. M. et al., 2013, ApJS, 209, 3
Lam D., Broadhurst T., Diego J. M., Lim J., Coe D., Ford H. C., Zheng W., 2014, ApJ, 797, 98
Lotz J. et al., 2014, Am. Astron. Soc. Meeting Abstr., 223, 254.01
McKee C. F., Ostriker E. C., 2007, ARA&A, 45, 565
Meneghetti M. et al., 2014, ApJ, 797, 34
Merten J. et al., 2015, ApJ, 806, 4
Neto A. F. et al., 2007, MNRAS, 381, 1450
Newman A. B., Treu T., Ellis R. S., Sand D. J., Nipoti C., Richard J., Jullo E., 2013, ApJ, 765, 24
Oesch P. A. et al., 2012, ApJ, 759, 135
Oesch P. A. et al., 2014, ApJ, 786, 108
Oguri M., 2007, ApJ, 660, 1
Oguri M., 2015, MNRAS, 449, L86
Peebles P. J. E., 2000, ApJ, 534, L127
Planck Collaboration XIII, 2015, preprint (arXiv:1502.01589)
Ponente P. P., Diego J. M., 2011, A&A, 535, A119
Postman M. et al., 2012, ApJS, 199, 25
Rau S., Vegetti S., White S. D. M., 2014, MNRAS, 443, 957
Refsdal S., 1964, MNRAS, 128, 307
Robertson B. E., Ellis R. S., Furlanetto S. R., Dunlop J. S., 2015, ApJ, 802, L19
Schive H.-Y., Chiueh T., Broadhurst T., 2014, Nature Phys., 10, 496
Sendra I., Diego J. M., Broadhurst T., Lazkoz R., 2014, MNRAS, 437, 2642
Sharon K., Johnson T. L., 2015, ApJ, 800, L26
Smith G. P. et al., 2009, ApJ, 707, L163
Treu T. et al., 2015 (arXiv:1510.05750)
Umetsu K. et al., 2014, ApJ, 795, 163
Zheng W. et al., 2012, Nature, 489, 406
Zheng W. et al., 2014, ApJ, 795, 93
Zitrin A., Broadhurst T., 2009, ApJ, 703, L132
Zitrin A. et al., 2013, ApJ, 762, L30
Zitrin A. et al., 2014, ApJ, 793, L12
Zitrin A. et al., 2015, ApJ, 801, 44

This paper has been typeset from a TeX/LaTeX file prepared by the author.